

See discussions, stats, and author profiles for this publication at: <https://www.researchgate.net/publication/222093717>

Blind deconvolution for high-resolution confocal scanning laser ophthalmoscopy

Article in *Journal of Optics A Pure and Applied Optics* · October 2005

DOI: 10.1088/1464-4258/7/10/010

CITATIONS

17

READS

43

3 authors:



Vincent Nourrit

Institut Mines-Télécom

25 PUBLICATIONS 203 CITATIONS

[SEE PROFILE](#)



Brian Vohnsen

University College Dublin

132 PUBLICATIONS 1,015 CITATIONS

[SEE PROFILE](#)



Pablo Artal

University of Murcia

367 PUBLICATIONS 10,160 CITATIONS

[SEE PROFILE](#)

Some of the authors of this publication are also working on these related projects:



ACTIVIDADES DE INVESTIGACION DEL LABORATORIO DE OPTICA DE LA UMU [View project](#)



Capsular bag stability of intraocular lenses [View project](#)

Blind deconvolution for high-resolution confocal scanning laser ophthalmoscopy*

V Nourrit, B Vohnsen and P Artal

Laboratorio de Óptica, Departamento de Física, Universidad de Murcia, Edificio C, Campus Espinardo (Edificio C), 30071 Murcia, Spain

E-mail: vnourrit@um.es

Received 9 March 2005, accepted for publication 28 July 2005

Published 9 September 2005

Online at stacks.iop.org/JOptA/7/585

Abstract

We investigate the potential of image deconvolution techniques, either in combination or as a substitute for adaptive optics, in a high-resolution confocal scanning laser ophthalmoscope (SLO). After reviewing the validity of standard hypotheses and the *a priori* information, we implement two deconvolution algorithms to be applied to experimental retinal images recorded with our own high-resolution research SLO. Despite the important assumptions, standard non-iterative or iterative techniques can improve on images (subtending from 1° to 5°), although the best results were obtained when deconvolution techniques were used in combination with adaptive optics. Low signal-to-noise ratio and blurring caused by eye movements are the main limiting factors for deconvolution techniques in this application.

Keywords: blind deconvolution, retinal imaging, adaptive optics, scanning laser ophthalmoscope

1. Introduction

Confocal scanning laser ophthalmoscopes (cSLOs) provide high-resolution and tomographic images of the living human retina [1, 2]. The lateral and axial resolution of the images is however limited due to the eye's aberrations [3]. A way to overcome this limitation is to use adaptive optics to correct for the ocular wavefront aberrations [4, 5], eventually together with a tiny confocal pinhole chosen to facilitate cone-mosaic imaging [6]. Nevertheless, while adaptive optics can improve the image quality in terms of resolution and contrast, it also increases the complexity and cost of the system. An alternative solution may be found in image deconvolution techniques, already proposed and in some cases successfully used in flood-illumination retinal imaging [7–10], conventional fluorescence confocal microscopy [11, 12], astronomy [13], etc.

In this work, the use of image restoration techniques for high-magnification cSLOs is addressed. Both non-iterative and iterative methods are examined for images obtained without, as well as with, adaptive optics. Actually, O'Connor *et al* [14] have also considered image reconstruction from an SLO, but with a set-up very different from ours. They used

fluorescent dye and recorded images that were 20 times larger than in the present study. Furthermore, their main interest was on iterative 3D deconvolution.

This paper is organized as follows: the experimental set-up is described in section 2. In section 3.1 the validity of classical assumptions (linear incoherent process with additive noise) is addressed, and in section 3.2 the *a priori* information used to regularize the problem is reviewed. The numerical procedures are presented in section 4, including denoising and deconvolution algorithms. We chose to implement two algorithms, one non-iterative, the other iterative, in order to illustrate the two main approaches among image deconvolution techniques. As it is difficult to estimate the experimental point spread function (PSF) accurately, both implemented algorithms are blind approaches, i.e. they reconstruct both the object and the PSF [15]. However, when a PSF is required to initiate the calculation process, an experimental one is used. Results are then presented and discussed in section 5. Finally, section 6 presents the conclusions.

2. Experimental set-up

We built our own cSLO (figure 1) with optional adaptive optics that allows for 512×512 pixel-sized images to be

* Part of the II EOS Topical Meeting on Physiological Optics (Granada, Spain, September 2004).

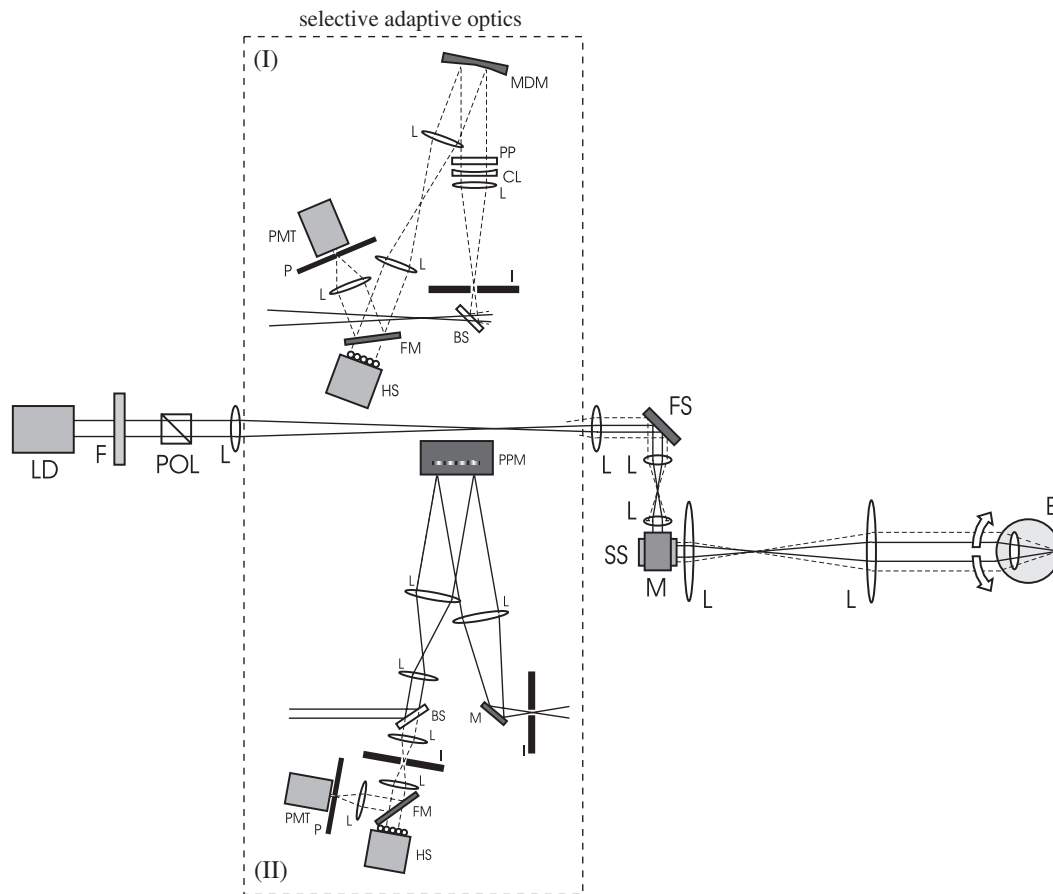


Figure 1. Diagram of the experimental set-up where the incident light path includes a laser diode or HeNe laser (LD), filter (F) and polarizer (POL), AR-coated achromats (L), beamsplitter (BS), fast (FS) and slow (SS) angular scanners, mirror (M), and eye (E). The returning light path includes an iris (I), cylindrical lens (CL) and phase plate (PP), membrane mirror (MDM) or programmable phase modulator (PPM), flip mirror (FM), Hartmann–Shack sensor (HS), pinhole (P), and photomultiplier tube (PMT). Dependent on the configuration either an adaptive system correcting (I) only the exit path or (II) both the entrance and the exit path of light to/from the eye can be chosen.

recorded by scanning in a raster pattern at ~ 15 Hz frame rate or alternatively for 256×256 at ~ 30 Hz [5]. For the illumination, either a near-IR laser diode ($\lambda = 785$ nm) or a yellow He–Ne laser ($\lambda = 594$ nm) has been used. In the latter case two drops of tropicamide have typically been used to dilate the pupil. To reduce image degradation by unwanted eye motion during scanning, the subject looked at a fixation target with the head position fixed by means of a bite bar. Defocus was corrected by adjusting the system lens closest to the eye together with the subject position, thereby avoiding loading the adaptive optics subsystem with the task of correcting it. The remnant aberrations were measured with a Hartmann–Shack wavefront sensor [16]. For the wavefront correction two types of adaptive elements have been tested. One is an aluminium-membrane mirror (Flexible Optical) that is deformed electrostatically by applying a set of 37 voltages to an underlying electrode pattern [17, 18]. The operational range of the mirror is restricted to aberrations less than ~ 0.5 μm and also limited by having to bias the mirror shape even in the absence of aberrations. Thus, to get the aberrations within the working range of the mirror, the system has been equipped with a cylindrical lens and a fourth order phase plate to reduce the amount of astigmatism, coma and spherical aberrations that are otherwise often present [19]. To reduce

complications with its control, the deformable mirror has been implemented in the cSLO so as to allow wavefront correction of only the light leaving the eye. The other element tested is a programmable phase modulator (Hamamatsu X8267 [20]), that although being slower in operation allows for a much better spatial control of the correction by virtue of its 1024×768 pixel display resolution. As compared to the mirror, this device permits larger aberrations to be corrected by wrapping the required phase in 2π segments although each shift at 2π produces some unwanted scattering. We have implemented this element in a double-passage scheme correcting both the beam entering the eye and the light re-emitted by the retina and exiting the eye, since this configuration eventually should allow for the highest resolving power. We used our cSLO to obtain images of the retina under the different conditions of magnification, location, type of aberration correction, etc. These images serve as a unique database for the application of the deconvolution strategies developed in this study.

3. Image formation

3.1. Assumptions

Several assumptions have to be made in order to be able to process our images using standard deconvolution methods.

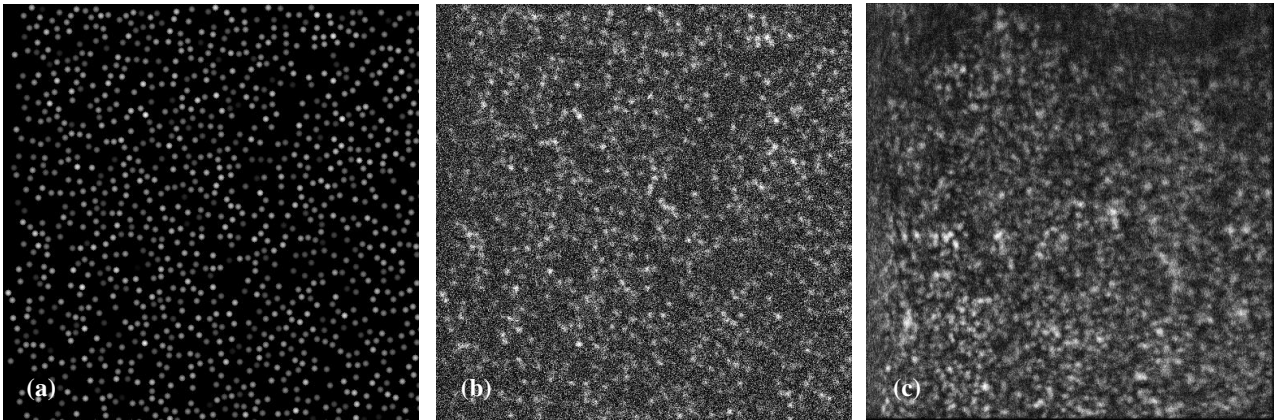


Figure 2. Simulation of the image degradation process. (a) Artificial retinal image of $1^\circ \times 1^\circ$; cones are $5 \mu\text{m}$ wide with a Gaussian intensity profile. (b) Convolution of (a) with an experimental PSF with additive noise. (c) $1^\circ \times 1^\circ$ large experimental image for comparison.

First, that the SLO images can be processed as normal extended images; i.e. we consider an image (I) to be a 2D convolution of the object (O) with the system point spread function (PSF) possibly influenced by additive noise (n):

$$I = O * \text{PSF} + n. \quad (1)$$

By assuming that the PSF is space invariant, we neglect the small spatial variations of the PSF due to the scanning. This also implies that our field of observation is in the isoplanatic range, which is justified by the small size of our images (1° – 5°) as compared to those studied by O'Connor *et al* (20°) [14]. It should be stressed that the assumed 2D image situation cannot be expected to discriminate against signal contributions from out-of-focus planes. This would require a definition of the 3D PSF of the system and would come closer to the ideal sought in an experimental situation with adaptive optics. However, the depth-selectivity of the confocal pinhole, together with the fact that most of the measured light originates at the photoreceptor layer or beyond (for near-IR illumination), supports somewhat the present hypothesis of single-plane imaging. Furthermore, in equation (1), we have assumed that the image formation phenomenon is incoherent, i.e. that the small spot of light on the retina does not create interference in the plane of the confocal pinhole. Although in the actual experiments the incident light is coherent, this assumption can be partly justified by the small illuminated area and the partial loss of coherence on the retina and during the back-propagation [21, 22]. Moreover, from [23] it is known that incoherent deconvolution of coherent images can still improve the quality. Image degradation of simulated retinal objects [24] following these assumptions provides images that are similar to experimentally recorded ones (figure 2).

3.2. *A priori* information

Image deconvolution is an ill posed inverse problem and consequently the quality of restoration depends typically on the *a priori* information available (to restore the well posedness). We do have a partial knowledge of the PSF as well as the object both in the Fourier space (where the spectrum of the image may exhibit spatial frequencies associated with the cone photoreceptor distribution [25, 26]) and in the real

space (anatomical data). We choose, however, to apply only the usual positivity constraint, not to restrict the class of admissible solutions. *A priori* information is used at the end of the reconstruction procedure to reject dubious images. For instance, the apparition of a Yellot's ring representative of the typical cone photoreceptors spacing [27] in an image recorded with too low resolution, would be evidence of an artefact and the corresponding cone spacing therefore faulty.

Information about the PSF is usually required to ensure regularization. In our case, measuring it non-invasively is not easily accomplished. It is also not feasible to extract it from an image as in standard fluorescent microscopy since there is no reliable image reference such as an isolated fluorescent marker of sub-resolution size. Defining one from an analytical model of the eye's PSF or optical transfer function (OTF) [28] would not necessarily provide a more accurate estimate. For this reason, we chose to implement blind deconvolution algorithms, i.e., algorithms that restore simultaneously both the object and the PSF. However, it should be stressed that in the case of blind deconvolution the initial PSF is experimentally defined on the basis of measurements with a Hartmann–Shack wavefront sensor.

Concerning the noise, the background measured in the absence of a subject is approximately 10 times lower than the signal measured from the eye. However, since the actual amount of signal related to the retina is unknown, and since there is no exact pixel-to-pixel correspondence between successively recorded images due to unwanted eye movements (see section 4.1), it is difficult to estimate the statistical characteristics of the signal. In the context of image processing, the noise is usually assumed to follow Gaussian or Poisson statistics. We chose not to assume any model in the non-iterative case, and Poisson statistics in the iterative case in order to be able to use a standard algorithm known to lead to positive results. The latter is justified when photon noise prevails over electronic noise in the detection system.

4. Image deconvolution

4.1. Preprocessing

Experimentally recorded images have to be preprocessed before deconvolution. This preprocessing consists of two

steps. First, images have to be spatially linearized in order to avoid image distortion produced by the non-linearity inherent in the scanner motion. Second, in order to be able to sum several images to improve the signal-to-noise ratio, images have to be spatially shifted to compensate for (at least partially) eye motion during imaging. Actually, although the subject is asked to fixate at a target during acquisition, random eye movements occur during fixation, which can perturbate the image acquisition process [29, 30]. These motions can typically be divided into three categories [31]: tremor, microsaccades and slow drift. Microsaccades are of approximately 25 ms duration and occur at 1–5 Hz. In the interval the eye drifts slowly (with an amplitude of up to 9 arcmin). These two movements are superimposed with high frequency (30–90 Hz) tremors.

Concerning tremors, their amplitude is small enough to be only disruptive for very high-resolution images. Actually, their maximum amplitude is approximately 30 arcsec, which corresponds to $1^\circ/120^\circ$, i.e., only 4.27 lines in a $1^\circ \times 1^\circ$ image with 512 lines. However, due to their high frequency with respect to the speed of scanning, such shifts can occur up to six times in a single image. In contrast, with a recording speed of 15 Hz, a microsaccade occurs only every four or five images but due to their more important amplitude (up to 20 arcmin) a microsaccade can be highly disruptive if occurring during image recording. An image is actually recorded in 66.6 ms (15 Hz) or 33.3 ms (30 Hz). A microsaccade could then shift the scanning point by as many as 170 lines in a $1^\circ \times 1^\circ$ image with 512 lines. Slow drifts are usually too slow to be disruptive, but it should be stressed that these values are mean values and larger values have been reported in the literature. For these reasons, it could be of relevance to monitor the trajectory of the visual fixation point simultaneously with the recording of an image.

In our case, since our system does not record images with a high enough frequency to guarantee that these movements do not affect the quality, a numerical correction has to be performed. This second step in the preprocessing is performed by looking for the maximum of correlation between successively recorded images; i.e., in contrast to O'Connor *et al* [14], we assume that eye motions only produce image translation. We do not consider rotational displacements since this increases greatly the computational time and because our scanning range is small. Furthermore, Wade *et al* [32] found that, in the context of high-magnification images with a low S/N ratio, rotation correction does not bring a significant improvement. Even then, however, the correction is only partial since deformations within each image cause a local deterioration with a negative influence on the summation process. Comparison of images (a), (b) and (d) in figure 3 illustrates the importance of correcting for eye movements while adding images, and also shows the increased blur in a fraction of the image when the number of added images is large (cf the improved quality of the upper right corner of the image with the increased blur at the lower left corner). The lachrymal film and the fact that the retina is not rigid but rather a semi-fluid surface may also have some influence on this local deterioration.

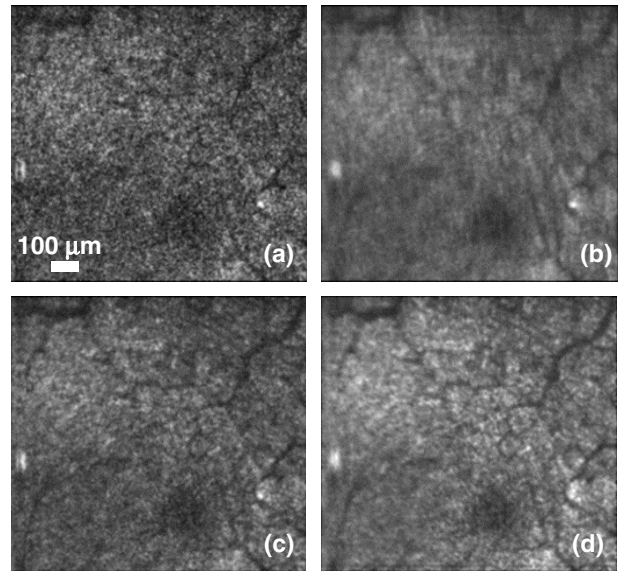


Figure 3. Effects of eye movements on image summation. (a) Single frame. (b) Direct sum of 16 frames. (c) Sum of four frames after partial correction of eye's movements. (d) Sum of 16 frames after partial correction of eye's movements.

4.2. Algorithms

We have assumed the distortion of the image to be a linear space invariant process. One could then expect to recover an approximation of the object (O') by calculating the inverse filter:

$$O' = \text{FT}^{-1} \left(\frac{\text{FT}(I)}{\text{FT}(\text{PSF})} \right) \quad (2)$$

where FT denotes the Fourier transform. Unfortunately, the image is noisy and inverse filtering amplifies the noise, particularly where the frequency response of the filter is small. Since the PSF is band limited and not well determined, the problem is ill posed. In this context, a large variety of deconvolution algorithms exist. We implemented two different algorithms: a direct method and an iterative one. Our goal is not to compare the pros and cons of each method [33] but rather to illustrate the fact that both can be successfully applied to retinal images. We briefly review both methods in sections 4.3 and 4.4.

4.3. Non-iterative method

More elaborate filters [34] than the one in equation (2) can be defined, such as the regression filter, the Wiener filter, the modified Wiener filter, etc, but in view of the low signal-to-noise ratio of our images, and the fact that the PSF is band limited and not perfectly known, such techniques do not perform well, creating at best photoreceptor-like artefacts.

Consequently, since the denominator in equation (2) is problematic, one solution is to consider for the OTF a well defined function. In this context, it should be mentioned that the PSF obtained experimentally by means of the wavefront sensor, however realistic it is, may not be the one that will allow numerically the best image improvement.

Thus, in view of the importance of a well estimated PSF for this to function, we considered the non-iterative blind

deconvolution method proposed by Carasso *et al* [35, 36]. Briefly, it supposes that the PSF belongs to a special class of function, namely radially symmetric Lévy-stable density functions, whose OTFs are defined by the equation

$$\text{OTF}(u, v) = \exp[-\alpha(u^2 + v^2)^\beta], \quad \alpha > 0, \quad 0 < \beta \leq 1. \quad (3)$$

Lévy densities are a large class of functions including Gaussian and Lorentzian densities, and a large variety of electro-optic devices have OTFs that are well described by equation (3) [35].

The method of Carasso *et al* (APEX method) allows recovery of parameters α, β from a 1D Fourier analysis of the image (assuming that the logarithm of the object spectrum presents a global behaviour that is generally monotonic, decreasing and convex). Then, once the PSF is estimated, a non-iterative standard deblurring method is used:

$$O' = \text{FT}^{-1} \left(\frac{\overline{\text{OTF}} \times \text{FT}(I)}{|\text{OTF}|^2 + K^{-2}|1 - \text{OTF}^s|^2} \right) \quad (4)$$

where K and s are positive constants based on *a priori* information (in the form of interactive trials) and where the symbol $\bar{}$ denotes the conjugate.

4.4. Iterative method

Iterative methods offer an alternative procedure. Among them, projection on to constraints algorithms (POCS) [15, 37] can be relatively easy to implement but unfortunately present well known problems of convergence. In contrast, Bayesian restoration offers a more robust mathematical background and has successfully been used in confocal microscopy [10]. Following this approach, we make use of a stochastic model of the imaging process. Then, I, O and PSF are viewed as probability density functions and the Bayes theorem gives

$$P(O|I) = P(I|O)P(O)/P(I) \quad (5)$$

where $P(O|I)$ is the *a posteriori* probability distribution, $P(I|O)$ the likelihood, $P(I)$ a normalization factor and $P(O)$ the *a priori* distribution.

If we suppose $P(X) = X_i/N$, where X_i is the value of the i th pixel in the array X and N the total number of pixels, the solution O of equation (5) can be obtained with the iterative procedure

$$O_{n+1} = O_n \left[\overline{\text{PSF}} * \left(\frac{I}{\text{PSF} * O_n} \right) \right] \quad (6)$$

where n is the number of iterations. This is the well known Richardson–Lucy algorithm but a similar expression can be obtained with the likelihood expectation–maximization approach considering a Poisson noise. The Poisson MAP method also gives a similar result [33]. Since this algorithm is unstable in the presence of noise and with an increasing number of iterations [38] we choose to add a regularizing constraint in the form of a maximum entropy constraint with Poisson noise statistics:

$$O_{n+1} = O_n \left[\overline{\text{PSF}} * \left(\frac{I}{\text{PSF} * O_n} \right) - T \log(O_n) + C_2 \right] C_1 \quad (7)$$

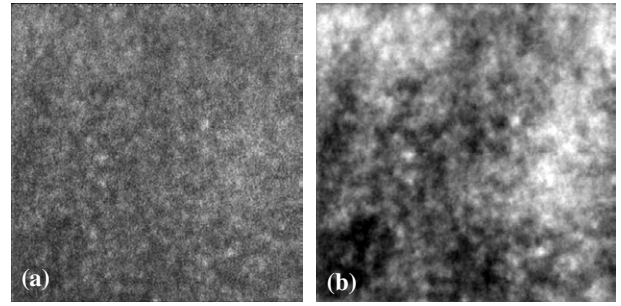


Figure 4. Application of the non-iterative method to an experimental image. (a) Experimental retinal image of $1^\circ \times 1^\circ$. (b) Deconvolution of image (a) with the non-iterative method.

i.e. we consider now $P(O) = \exp(TS(O))$, with T a positive parameter and $S(O)$ the entropy. In this expression, C_1 is a normalization factor, C_2 is a positive constant chosen so that $O_{n+1} > 0$ and T can be seen as an adjustable parameter to weight the regularizing constraint. For small T we retrieve the Richardson–Lucy algorithm and its noise amplification for large n . For large T we smooth the reconstructed object and lose high spatial frequencies.

In the case of blind deconvolution the PSF is re-estimated at each iteration with the equation

$$\text{PSF}_{n+1} = \text{PSF}_n \left[\overline{O_n} * \left(\frac{I}{\text{PSF}_n * O_n} \right) \right]. \quad (8)$$

Here, the initial estimate for the PSF (i.e., PSF_0) is the experimentally established one based on a measurement of the remnant wavefront aberrations. This is of particular importance for the convergence of the iterative process.

5. Results of deconvolution

The purpose of deconvolution is to improve image quality to facilitate the identification of various elements and ultimately to recover lost spatial frequencies. Here we describe the outcome of applying non-iterative and iterative methods respectively on cSLO images. As already stated (section 3.2) we use *a priori* information to assess the consistency of the results.

5.1. Non-iterative method

After validating our algorithm on synthetic images (for simplicity not shown here), we applied it to experimental data (figure 4). It appears that this method allows an increase of the contrast and the overall quality of the image but without a significant resolution improvement. The contrast improvement is supported by the comparison of the grey scale histograms for the images before and after deconvolution (figure 5). In order to calculate the contrast we do not use Michelson's formula since both images contain pixels with zero (minimum) or unit (maximum) values. Instead, we make use of the root mean square contrast, defined as the standard deviation, relative to the mean, of the intensity values of each pixel in the image [39]. In this case, the rms contrast improvement is then 92.9%.

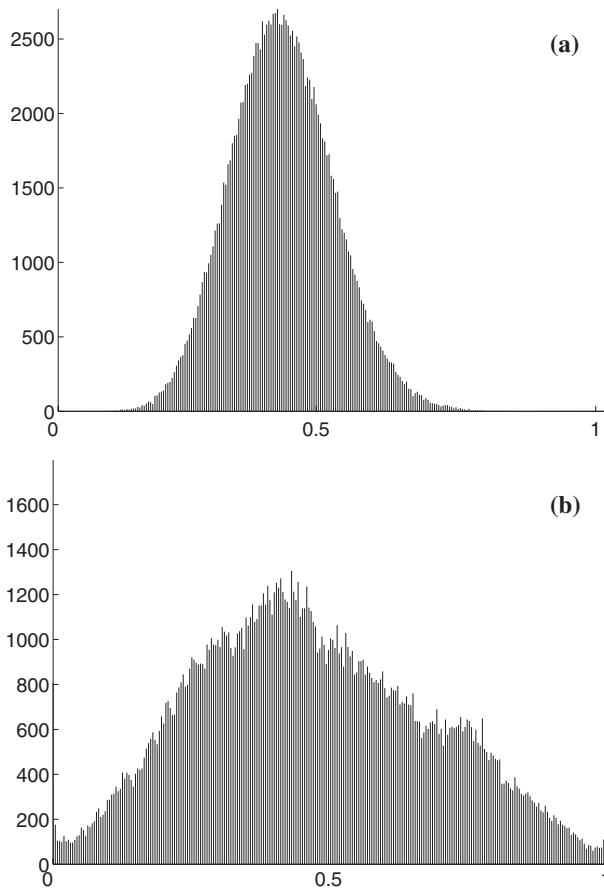


Figure 5. (a) Histogram of grey levels for image 4(a).
(b) Histogram of grey levels for image 4(b).

The overall quality of the image is improved but the deconvolution does not allow one to distinguish finer details. This may possibly be explained by the fact that asymmetries of the PSF are not taken into account. The technique may be applied as a fast contrast-enhancing method, for instance to facilitate detection of particular features such as small capillaries.

5.2. Iterative method

The iterative method also allows the image quality to be improved (figure 6), but again without a significant improvement in resolution. In order to illustrate the contrast improvement, figure 7 presents the histograms of grey scales for the images pre- and post-deconvolution (figures 6(a) and (b)). In this case the improvement in rms contrast is 13%.

The lack of improvement in resolution can be explained by two different factors. First, the image deterioration (cf section 4.1) blurs irreparably the image. Second, at high noise levels iterative methods are shown to diverge and little is known about the error estimates and convergence rates of probabilistic algorithms [33]. Thus adding a regularization constraint implies a compromise between image smoothening and the maintenance of high frequency contents together with more noise (consequently balancing the credibility of very small structures).

Since both the non-iterative and the iterative methods have a limited impact on the image restoration in terms of resolution,

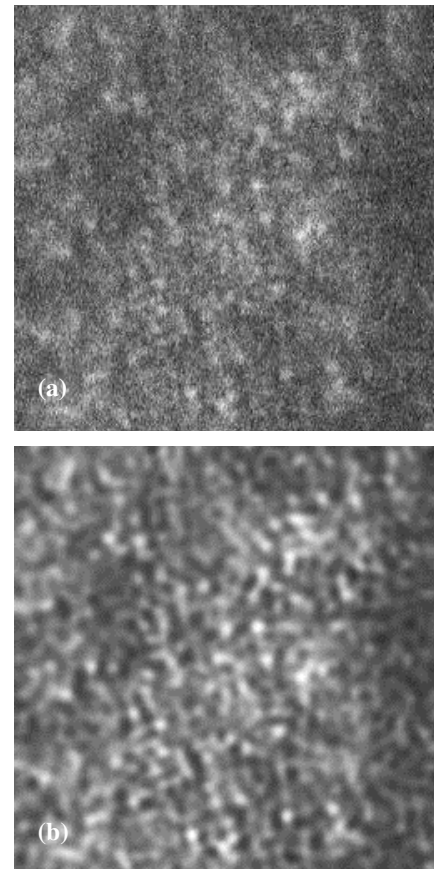


Figure 6. Application of the iterative method to experimental images of $0.5^\circ \times 0.5^\circ$. (a) Original images; (b) deconvolution.

they are both preferably suited in complement to adaptive optics (figure 8). Adaptive optics allows not only an improved signal-to-noise ratio, one of the main limiting factors, but also a smaller illuminated area at the retina (when correcting the incident beam as in figure 1, part II), in better agreement with the assumptions of the present model. Moreover, by improving the focus, adaptive optics may reduce the impact of scattering from out-of-focus sources on the PSF as well as on the images.

The improvement in rms contrast between figures 8(a) and (b) is 21.9% and 10.2% between figure 8(a) and its corresponding part in figure 8(c) (due to adaptive optics only). Concerning the deconvolution of figure 8(c), we have already obtained a contrast improvement of 13% (figure 6(b)). Figure 8(d) differs from figure 6(b) as we have applied different parameters during the deconvolution (mainly a different T value). As a result, the contrast is lower (-22%) than in figure 8(c). Nevertheless, careful calculation of the image spectral density after processing shows increased contributions at frequencies around the Yellot ring (figure 9) supporting the direct improvement in the processed images (figure 8(d)) with an improved visibility of photoreceptors. Actually, the image has been recorded at approximately 1.5° eccentricity, hence in a region where the expected cone spacing would be about $5.4 \mu\text{m}$ [40]. This is in fair agreement with the increase by a factor 3 in signal (for the power spectrum) in the area around 50 cycles/degree (highlighted by an arrow in figure 9(b)) corresponding to a cone spacing of $5.6 \mu\text{m}$ (with

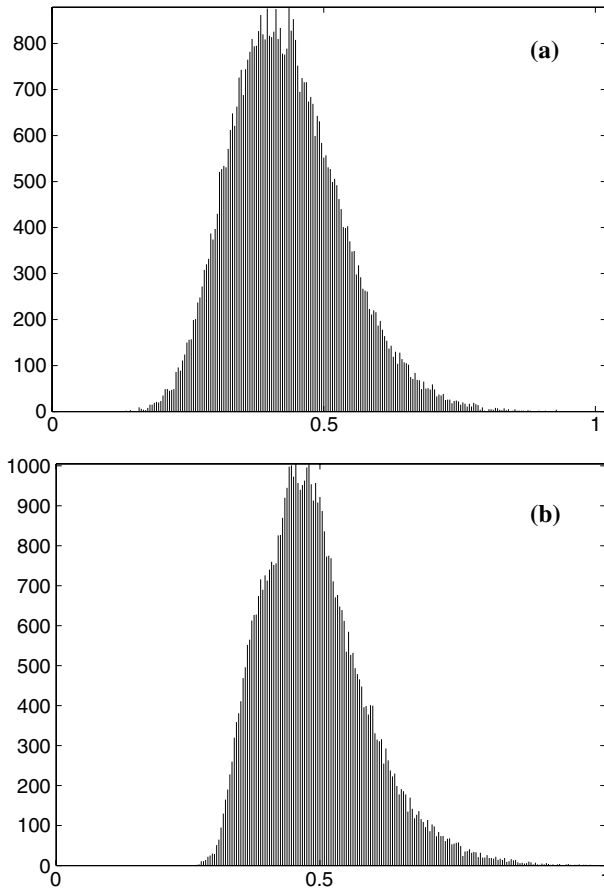


Figure 7. (a) Histogram of grey levels for image 6(a).
(b) Histogram of grey levels for image 6(b).

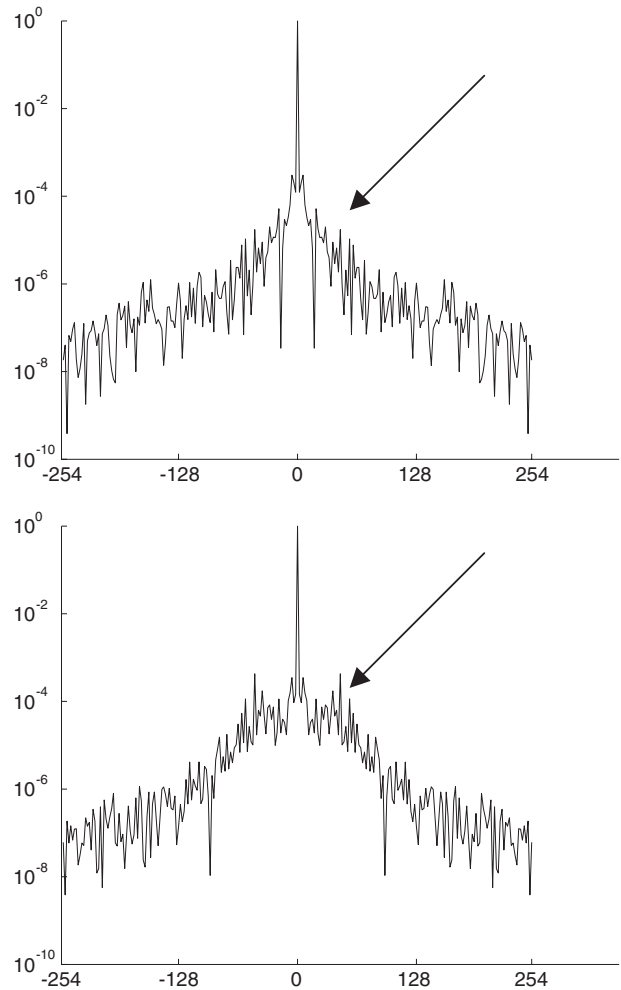


Figure 9. Section along the horizontal axis of the spectral density: (a) of image 8(c) and (b) of image 8(d) illustrating the increased values for spectral frequencies in the Yellot's ring. The abscissa axis is in cycles/degree. Profiles in the perpendicular direction are similar.

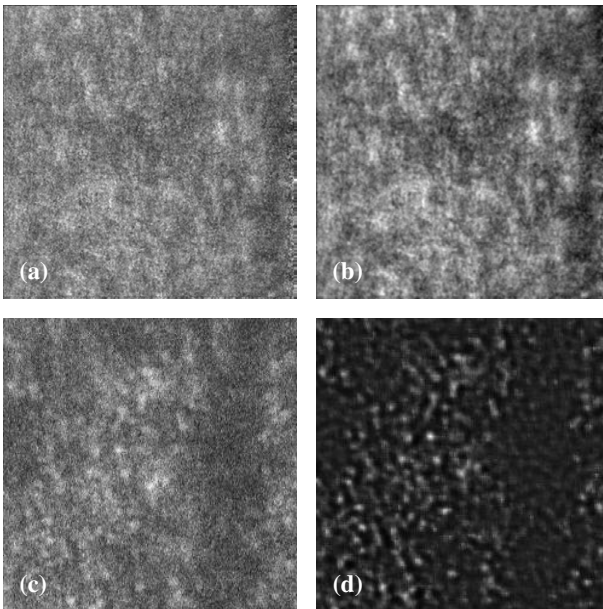


Figure 8. Performance of deconvolution techniques on images recorded without or with adaptive optics. (a) Experimental image recorded without adaptive optics. Image (a) is $1^\circ \times 1^\circ$ in size. (b) Deconvolution of image (a) with the non-iterative method. (c) Experimental image recorded with adaptive optics. Image (c) is $0.5^\circ \times 0.5^\circ$ in size and corresponds to a portion of image (a). (d) Deconvolution of image (c) with the iterative method.

a conversion factor of $280 \mu\text{m}/\text{deg}$). Further studies are still needed, however, in order to test the reliability of the method at other retinal locations where the cone photoreceptor density differs from the present case.

6. Conclusion

We reviewed and assessed, in the context of the cSLO, the validity of assumptions associated with standard 2D deconvolution techniques as well as the *a priori* information for regularization. Despite important assumptions, standard deconvolution techniques, iterative or non-iterative, can be used to improve images from a cSLO. Super-resolution, i.e., reconstruction of lost spatial frequencies, does not seem feasible, but the image contrast can be improved sufficiently to facilitate feature discrimination. We also reviewed potential noise sources in these types of images. Some of the main limiting factors are the signal-to-noise ratio and blurring caused by eye movements. The importance of these factors on the quality of the restoration has several consequences. First, in our application, and possibly others in which the

signal-to-noise ratio is a limitation, deconvolution techniques appear to be better used as a complement to adaptive optics than as a stand-alone image enhancement method. Second, a compromise has to be found between averaging several images to increase the signal-to-noise ratio and the related local image degradation due to eye movements. Thus, the advantage of recording high-resolution images contrasts with the effects caused by eye motion during scanning. Possible improvements on theory would be to assess more accurately the image formation model, and, on the experimental side, to increase the velocity of the scanning and/or to develop more sophisticated numerical techniques to compensate for unwanted eye motions.

Acknowledgments

This research was supported by the European Training Network Sharp-Eye, the Ministerio de Ciencia y Tecnología (Spain), grant BFM2001-0391 and red FIS G03/185.

The authors would also like to thank the anonymous reviewers for helpful comments that allowed us to improve the quality of the manuscript significantly.

References

- [1] Webb R H, Hughes G W and Delori F C 1987 Confocal scanning laser ophthalmoscope *Appl. Opt.* **26** 1492–9
- [2] Vieira P, Manivannan A, Lim C, Sharp P and Forrester J V 1999 Tomographic reconstruction of the retina using a confocal laser ophthalmoscope *Physiol. Meas.* **20** 1–19
- [3] Artal P, Guirao A, Berrio E and Williams D R 2001 Compensation of corneal aberrations by internal optics in the human eye *J. Vis.* **1** 1–8
- [4] Roorda A, Romero-Borja F, Donnelly W J III, Queener H, Hebert T J and Campbell M C W 2002 Adaptive optics laser scanning ophthalmoscopy *Opt. Express* **10** 405–12
- [5] Vohnsen B, Iglesias I and Artal P 2003 Confocal scanning laser ophthalmoscope with adaptive optical wavefront correction *Proc. SPIE* **4964** 24–32
- [6] Vohnsen B, Iglesias I and Artal P 2004 Directional imaging of the retinal cone mosaic *Opt. Lett.* **29** 968–70
- [7] Iglesias I and Artal P 2000 High-resolution retinal images obtained by deconvolution from wave front sensing *Opt. Lett.* **25** 1804–6
- [8] Arines J and Bará S 2003 Hybrid technique for high resolution imaging of the eye fundus *Opt. Express* **11** 761–6
- [9] Catlin D and Dainty C 2002 High-resolution imaging of the human retina with a Fourier deconvolution technique *J. Opt. Soc. Am. A* **19** 1515–23
- [10] Christou J C, Roorda A and Williams D R 2004 Deconvolution of adaptive optics retinal images *J. Opt. Soc. Am. A* **21** 1393–401
- [11] Boutet de Monvel J, Le Calvez S and Ulfendahl M 2001 Image restoration for confocal microscopy: improving the limits of deconvolution, with application to the visualization of the mammalian hearing organ *Biophys. J.* **80** 2455–70
- [12] Verveer P J, Gemkow M J and Jovin T M 1999 A comparison of image restoration approaches applied to three-dimensional confocal and wide field fluorescence microscopy *J. Microsc.* **19** 50–61
- [13] Primot J, Rousset G and Fontanella J C 1990 Deconvolution from wave-front sensing: a new technique for compensating turbulence-degraded images *J. Opt. Soc. Am. A* **7** 1598–608
- [14] O'Connor N J, Bartsch D U, Freeman W and Holmes T J 1998 Motion-compensated blind deconvolution of scanning laser ophthalmoscope imagery *Proc. SPIE* **3261** 71–87
- [15] Ayers G R and Dainty J C 1988 Iterative blind deconvolution method and its applications *Opt. Lett.* **13** 547–9
- [16] Prieto P M, Vargas-Martín F, Goelz S and Artal P 2000 Analysis of the performance of the Hartmann–Shack sensor in the human eye *J. Opt. Soc. Am. A* **17** 1388–98
- [17] Fernández E J, Iglesias I and Artal P 2001 Closed-loop adaptive optics in the human eye *Opt. Lett.* **26** 746–8
- [18] Fernández E J and Artal P 2003 Membrane deformable mirror for adaptive optics: performance limits in visual optics *Opt. Express* **11** 1056–69
- [19] Ftaclas C, Basedow R, Nonnenmacher A, Weindling F, Story D and Nelan E 1993 Hubble space telescope fine-guidance-sensor transfer function and its impact on telescope alignment and guidance *Appl. Opt.* **32** 1696–702
- [20] Prieto P M, Fernández E J, Manzanera S and Artal P 2004 Adaptive optics programmable phase modulator: applications in the human eye *Opt. Express* **12** 4059–71
- [21] Artal P, Marcos S, Navarro R and Williams D R 1995 Odd aberrations and double-pass measurements of retinal image quality *J. Opt. Soc. Am. A* **12** 195–201
- [22] Diaz-Santana L and Dainty J C 2001 Effects of retinal scattering in the ocular double-pass process *J. Opt. Soc. Am. A* **18** 1437–44
- [23] Marcos S and Navarro R 1996 Imaging the foveal cones in vivo through ocular speckle interferometry: theory and numerical simulations *J. Opt. Soc. Am. A* **13** 2329–40
- [24] Ahumada A J Jr and Poirson A 1987 Cone sampling array models *J. Opt. Soc. Am. A* **4** 1493–502
- [25] Yellot J I 1982 Spectral analysis of spatial sampling by photoreceptors: topological disorder prevents aliasing *Vis. Res.* **22** 1205–10
- [26] Curcio C A, Sloan K R, Kalina R E and Hendrickson A E 1990 Human photoreceptor topography *J. Comp. Neurol.* **292** 497–523
- [27] Artal P and Navarro R 1989 High-resolution imaging of the living human fovea: measurement of the intercenter cone distance by speckle interferometry *Opt. Lett.* **14** 1098–100
- [28] Ijspeert J K, Van den Berg T J T P and Spekreijse H 1993 An improved mathematical description of the foveal visual point spread function with parameters for age, pupil size and pigmentation *Vis. Res.* **33** 15–20
- [29] Hart W M (ed) 1994 *Adler's Physiology of the Eye*
- [30] Hammer D X, Ferguson R D, Magill J C, White M A, Elsner A E and Webb R H 2003 Compact scanning laser ophthalmoscope with high-speed retinal tracker *Appl. Opt.* **42** 4621–32
- [31] Bartsch D U and Freeman W R 1993 Laser-tissue interaction and artifacts in confocal scanning laser ophthalmoscopy and tomography *J. Neurosci. Biobehavioral Rev.* **17** 459–67
- [32] Wade A R and Fitzke F W 1998 A fast, robust pattern recognition system for low light level image registration and its application to retinal imaging *Opt. Express* **3** 190–7
- [33] Carasso A S 1999 Linear and nonlinear image deblurring: a documented study *SIAM J. Numer. Anal.* **36** 1659–89
- [34] Arines J and Bará S 2000 Significance of the recovery filter in deconvolution from wavefront sensing *Opt. Eng.* **39** 2789–96
- [35] Carasso A S, Bright D S and Vladár A E 2002 APEX method and real-time blind deconvolution of scanning electron microscope imagery *Opt. Eng.* **41** 2499–514
- [36] Carasso A S 2001 Direct blind deconvolution *SIAM J. Appl. Math.* **61** 1980–2007
- [37] Kotzer T, Cohen N and Shamir J 1998 Generalized projection algorithms with applications to optics and signal restoration *Opt. Commun.* **156** 77–91
- [38] Llacer J and Nuñez J 1994 Ghost images and feasibility of reconstruction with the Richardson–Lucy algorithm *Proc. SPIE* **2302** 207–21
- [39] Peli E 1990 Contrast in complex images *J. Opt. Soc. Am. A* **7** 2032–40
- [40] Marcos S, Navarro R and Artal P 1996 Coherent imaging of the cone mosaic in the living human eye *J. Opt. Soc. Am. A* **13** 897–905